

RESEARCH ARTICLE

Wake meandering effects on floating wind turbines

Adam S. Wise¹  | Erin E. Bachynski² 

¹Department of Civil and Environmental Engineering, University of California, Berkeley, CA 94720, USA

²Department of Marine Technology, Norwegian University of Science and Technology, Trondheim, Norway

Correspondence

Erin E. Bachynski, Department of Marine Technology, Norwegian University of Science and Technology, Trondheim 7491, Norway.
Email: erin.bachynski@ntnu.no

Present Address

Adam S. Wise, Department of Civil and Environmental Engineering, University of California, Berkeley, Berkeley, CA 94720 USA

Abstract

As more floating farms are being developed, the wake interaction between multiple floating wind turbines (FWTs) is becoming increasingly relevant. FWTs have long natural periods in certain degrees of freedom, and the large-scale movement of the wake, known as wake meandering, occurs at very low frequencies. In this study, we use FAST.Farm to simulate a two-turbine case with three different FWT concepts: a semisubmersible (semi), a spar, and a tension leg platform (TLP), separated by eight rotor diameters in the wind direction. Since wake meandering varies depending on the environmental conditions, three different wind speeds (for all three concepts) as well as two different turbulence levels (for the semi) are considered. For the below-rated wind speed, when wake meandering was most extreme, yaw motion standard deviations for the downstream semi were approximately 40% greater in high turbulence and over 100% greater in low turbulence when compared with the upstream semi. The low yaw natural frequency (0.01 Hz) of the semi was excited by meandering, while quasi-static responses resulted in approximately 20% increases in yaw motion standard deviations for the spar and TLP. Differences in fatigue loading between the upstream and downstream turbines for the mooring line tension and tower base fore-aft bending moment mostly depended on the velocity deficit and were not directly affected by meandering. However, wake meandering did affect fatigue loading related to the tower top yaw moment and the blade root out-of-plane moment.

KEYWORDS

coherence, dynamic wake meandering, fatigue, floating wind turbine, wind farm modeling

1 | INTRODUCTION

Floating wind turbines (FWTs) are an emerging technology to harness the wind resource in deep water where bottom-fixed turbines are no longer economically viable. There have been several demonstration projects of stand-alone FWTs, but there is only one floating wind farm, Hywind Scotland.¹ Several other floating wind farms are currently in the planning stage, and as more floating wind farms are developed, modeling the wake interaction between FWTs is becoming increasingly relevant.

Wind turbine operation induces a downstream decrease in wind speed and an increase in turbulence intensity in the form of a wake. There are many observations of the effect of the wake on power production and structural loading.^{2–7} Moreover, the wake tends to meander in certain atmospheric conditions. This large-scale movement of the wake was observed as early as the 1980s by Ainslie.⁸ Ainslie noticed that variability in wind direction gave rise to meandering, particularly in nonstable atmospheric conditions. Recent high- and mid-fidelity simulations^{9,10} have also shown that wake meandering depends on atmospheric stability. In addition to atmospheric stability, wake meandering is likely to vary due to wind speed, turbulence, shear, veer, etc.

Wakes are commonly modeled with computationally inexpensive steady, or quasi-steady, wake modeling tools to optimize wind farm layout with respect to annual energy production. However, while these low-fidelity models can model performance in terms of power, they do not take into account structural loading (also relevant when calculating cost of energy) and fail to capture important wake dynamics such as meandering. High-fidelity large-eddy simulations (LESs) are currently the most accurate way to model wakes and can be coupled with aeroelastic simulation tools to provide information on structural loading. However, this approach is computationally prohibitive in an iterative structural design process.

This is an open access article under the terms of the Creative Commons Attribution License, which permits use, distribution and reproduction in any medium, provided the original work is properly cited.

© 2020 The Authors. Wind Energy Published by John Wiley & Sons, Ltd.

Recently, there has been success modeling wake dynamics using less computationally expensive mid-fidelity methods where a dynamic wake meandering (DWM) model is coupled with an aeroelastic simulation tool. In a DWM model, the wake flow field is treated using a splitting of scales methodology where turbulent eddies greater than two diameters affect wake meandering and those smaller than two diameters affect the wake-deficit evolution. A DWM model typically includes three submodels:

Velocity deficit — a steady-state wake-deficit model based on the axisymmetric thin-shear-layer approximation of the Navier-Stokes equation with an eddy-viscosity model for turbulence closure.⁸

Wake meandering — a wake-transport model of the wake deficit as a result of large-scale atmospheric turbulence, as a passive tracer.

Wake-added turbulence — a wake-turbulence model to account for the added turbulence introduced by the wake.

This model was first proposed by Larsen et al¹¹ and has recently been adopted into the annex of the fourth edition of the IEC 61400-1 standard.¹² The Larsen model coupled with HAWC2¹³ has been validated against operational wind farm measurement data and LES.¹⁴

Another tool that implements a DWM model with aeroelastic simulation is FAST.Farm, which is developed by the National Renewable Energy Laboratory (NREL).¹⁵ Instances of OpenFAST (formerly known as FAST¹⁶) within FAST.Farm model the nonlinear, dynamic behavior of distinct turbines. Wake dynamics are based on the principles of the DWM model but with some differences to address limitations in existing DWM implementations.¹⁵ Especially important for FWTs, FAST.Farm includes platform motions when updating the wake deficit and center line. FAST.Farm has been validated against LES for a number of cases, which have also been used to calibrate a number of wake dynamics parameters.^{17,18} A limitation of FAST.Farm in its current state is that wake-added turbulence is not yet implemented. However, previous research on wakes has found that added-wake turbulence has only a minor contribution to the total turbulence where increased turbulence is due almost exclusively to meandering of the velocity deficit¹⁴ and that ambient turbulence tends to dominate in the far-wake region¹⁹ (the region within the scope of the present work).

While FAST.Farm was originally developed to compute the ambient wind farm wide using a precursor LES, recent updates allow the inflow to be generated using synthetic turbulent wind models. The advantage of these spectral models is their limited computational expense, but they are most applicable for smaller wind farms.²⁰ Two synthetic turbulent wind models are specified by design standards¹²: the Kaimal spectral and exponential coherence model²¹ and the Mann uniform shear model.^{22,23} While the two different turbulence models have little impact on the simulated responses for bottom-fixed and onshore wind turbines, the two models result in significantly different responses for FWTs.^{24–27} The frequency content of both models follows that of the Kaimal spectrum, but the spatial variation of the wind field differs. The spatial coherence in the Kaimal model is fit empirically using an exponential function while the Mann model generates turbulence using a spectral tensor, resulting in spatial coherence in all three wind directions. Inflow generated using the Kaimal model has been compared with LES in FAST.Farm and was shown to reasonably predict meandering.²⁸ The aforementioned validation study¹⁴ of DWM in HAWC2 used inflow generated with the Mann model. While both inflow methods have been shown to accurately capture meandering, there are some differences in wake meandering that can have an effect on low-frequency FWT dynamics.²⁹ The present work does not attempt to determine whether one model is more correct than the other, which would require extensive measurement data, but to compare their effect on the behavior of the wakes and the resulting response of the downstream turbine.

The major research question is how the slow meandering movement of wakes, which can vary due to a number of factors, affects floating wind turbines, which are structures with long natural periods in certain degrees of freedom. To answer this question, FAST.Farm is used to simulate two floating wind turbines separated in the stream-wise direction by eight rotor diameters (D). The upstream turbine operates under ambient, free-stream conditions while the second turbine operates in waked conditions. Three different FWT concepts, each supporting the DTU 10-MW reference wind turbine, are used: a semisubmersible, a spar, and a tension leg platform (TLP). To provide a comprehensive understanding of wake meandering effects, the environmental conditions include three different wind speed scenarios and two different turbulence levels. Additionally, synthetic inflow is generated using both the Kaimal turbulence model and the Mann turbulence model. In Section 2, we describe the OpenFAST models of the FWTs and the FAST.Farm model of the two-turbine case. Environmental conditions, including the inputs for the different methods used to generate synthetic turbulent inflow, are described in more detail in Section 3. Representative operational conditions were chosen in order to directly investigate the effects of wakes on motions and on short-term damage equivalent loading in the blade root, tower, and mooring lines. Simulation results are presented in Section 4, followed by conclusions in Section 5.

2 | NUMERICAL SIMULATION

2.1 | Dynamic analysis tool

FAST.Farm is an extension of the widely used aero-hydro-servo-elastic tool OpenFAST (formerly known as FAST). FAST.Farm incorporates instances of OpenFAST together with wake dynamics and ambient wind and array effects modules to capture the wake interaction within a wind farm. A low-resolution wind domain (in space and time) of the entire wind farm is used for resolving wakes, while a high-resolution domain around each wind turbine is used to accurately compute structural loading.

To calculate wind turbine dynamics, OpenFAST operates in a similar manner as for a single wind turbine simulation. OpenFAST includes modules for computing structural dynamics, aerodynamic loads, control and electrical-drive dynamics, hydrodynamic loads, and mooring system dynamics. Aerodynamic loads on the blades are computed using blade-element/moment theory while hydrodynamic loads on the rigid hull are computed using a combination of first-order potential flow (from WAMIT) and either Morison's equation (for the spar and TLP) or linear and

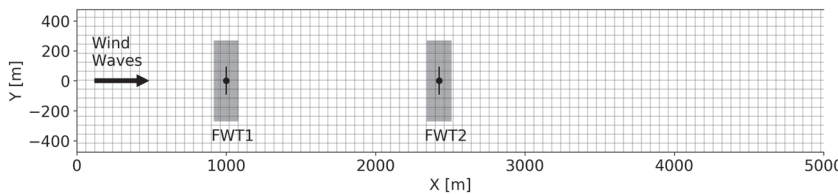


FIGURE 1 FAST.Farm low-resolution domain with the high-resolution domain around each floatingwind turbine (FWT) for an 8-m/s wind speed. For visualization, the low-resolution domain has been truncated to 5 km, and the grid spacing has been downsampled by a factor of 8 in both domains

quadratic global damping matrices (for the semi). Only linear waves, realized in accordance with the IEC 61400-3 standard,³⁰ are considered in this study. Each FWT computational model makes use of the MoorDyn³¹ mooring module, which utilizes a lumped mass model. Additionally, each FWT interfaces with its own collective blade pitch and generator torque controller. More detail on the OpenFAST models can be found in Section 2.2.

The FAST.Farm model uses a $X \times Y \times Z = 10 \times 952.5 \times 472.5$ -m domain and a simulation time length of 4000 seconds (including a 400-second start-up/transient). The main flow direction is along X with the upstream turbine, FWT1, located 1 km from the left boundary and the downstream turbine, FWT2, located 8D further downstream. The longitudinal length of the domain needs to be sufficiently large enough for the wakes to propagate downstream, and the lateral and vertical dimensions need to be large to allow for meandering of the wakes. The wake discretization consists of 160 wake planes per rotor, each with a radial finite-difference spatial resolution of 5 m.

The low-resolution wind domain used for resolving wakes has a spatial resolution of $\Delta Y = \Delta Z = 7.5$ m (corresponding to 128 and 64 grid points in the lateral and vertical directions, respectively) and a time step of 2 seconds. The high-resolution wind domain around each FWT has the same spatial resolution, but the temporal resolution is increased to 0.125 second. The spatial resolution of 7.5 m corresponds to the chord length of the DTU 10 MW to ensure accurate computation of structural loading and a time step of 0.125 second corresponds to a Nyquist frequency greater than the second tower frequency of all three models. Shaler et al³² provide more detailed guidance regarding inflow discretization. A schematic of the FAST.Farm low- and high-resolution domains can be found in Figure 1.

2.2 | FWT concepts

The three FWT aero-hydro-servo-elastic models each support the DTU 10-MW reference wind turbine.³³ The important characteristics of the DTU 10 MW are listed in Table 1. The DTU 10 MW was developed as an onshore model but has been adapted for offshore models in various studies. Because the tower bending frequency of the onshore tower increases for floating wind turbines, the tower design is generally modified to avoid resonance at the blade-passing (3P) frequency. While the structural properties of the tower are modified, the hub height for the FWTs is identical to that of the onshore model, 119 m above the still water line (SWL). More details on the specific modifications for each FWT in the present work are described in Sections 2.2.1 to 2.2.3, and visualizations in OpenFAST can be seen in Figure 2.

The semisubmersible concept and numerical model used in the present work were developed in OpenFAST as part of the Lifes50+ project^{34,35}; however, the spar³⁶ and TLP³⁷ were developed by the Norwegian University of Science and Technology (NTNU) in SINTEF Ocean's SIMA software and converted to the FAST framework.

These three concepts were chosen as they are representative of the three physical principles used to achieve static stability for offshore structures.³⁸ The stochastic amplitude and frequency of FWT motions strongly depend on the substructure, so choosing floating platforms with varied natural frequencies provides for a more comprehensive analysis. The semisubmersible concept is buoyancy stabilized, leading to very long natural periods in surge and yaw and a shorter natural period in pitch. The spar concept is ballast stabilized, leading to a similarly long natural period in surge, but has a much shorter natural period in yaw due to its small inertia. The TLP is stabilized using the mooring line tendons, resulting in minimal heave and pitch motions and a shorter natural period in surge compared with the semisubmersible and spar.

Selected characteristics for each FWT platform and mooring system are listed in Tables 2 and 3. The mooring system layout for each wind turbine is shown in Figure 3.

The blade pitch and generator torque controllers for the TLP have not been modified from those of the land-based concept; however, the blade pitch controllers for the semisubmersible and spar have been modified to avoid negative feedback at the platform pitch natural frequency.³⁹ Additionally, the semisubmersible and spar use a constant generator torque strategy in above-rated conditions to limit low-frequency dynamic responses. The yaw controller is not implemented in the present work. The gains, natural frequency, and above-rated strategy of the controllers are summarized in Table 4.

Parameter	Value
Rated power	10 MW
Rotor orientation and configuration	Upwind, three blades
Rotor, hub diameter	178.3 and 5.6 m
Cut-in, rated, cut-out wind speed	4.0, 11.4, and 25.0 m/s
Cut-in, rated rotor speed	6.0 and 9.6 rpm
Rotor, nacelle mass	230.7 and 446.0 tonnes

TABLE 1 Main characteristics of the DTU 10-MW reference wind turbine⁵⁴

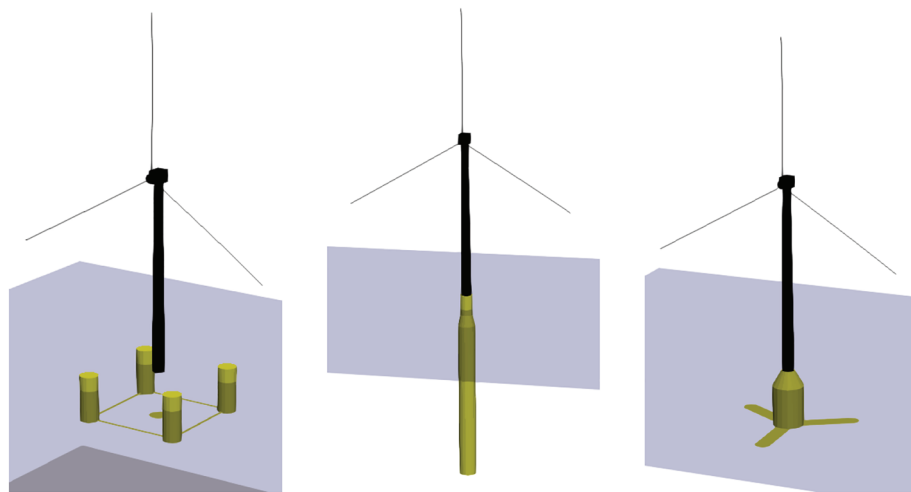


FIGURE 2 Computational models of the semi (left), spar (middle), and tension leg platform (TLP) (right) visualized in OpenFAST with lines representing the prebent blades. The tower and rotor are colored in black while the hydrodynamic members are colored in yellow [Colour figure can be viewed at wileyonlinelibrary.com]

2.2.1 | Semisubmersible platform

The Lifes50+ Nautilus semisubmersible platform⁴⁰ has four vertical columns that are connected using a quadratic ring base pontoon and by an integrated cross-shaped deck at the top (deck not shown in Figure 2). The platform is moored with four catenary steel chains connecting the midpoint of each column to the seabed 130 m below.

The natural frequencies and periods for the Nautilus are listed in Table 5. The Nautilus is characterized by very long natural periods in surge and yaw. The tower connects to the deck at 7.7 m above the SWL and is approximately 900 tonnes, roughly 1.5 times heavier than the towers on the other FWT concepts. This design results in a stiff-stiff tower, where the natural frequency of 0.526 Hz lies above the 3P range.

2.2.2 | Spar platform

The NTNU 10-MW spar platform has the same draft of 120 m as the 5-MW OC3-Hywind⁴¹ and is similarly designed for a water depth of 320 m, but the diameter of the lower and upper columns has been increased to provide additional buoyancy for the heavier 10-MW turbine and to match the tower base diameter.

The mooring system includes three catenary mooring lines. Characteristic of offshore structures attached to catenary mooring lines, similar to the semi, the spar has a long natural period in surge (see Table 6). In reality, a delta connection would be used to connect the fairleads with the hull to provide additional yaw stiffness. However, these bridles are not modeled, and an additional yaw spring stiffness of 1.48×10^8 Nm/rad is artificially added to the model.

The platform connects to the tower at 10 m above the SWL requiring the tower to be modified from that of the onshore design to achieve a hub height of 119 m. In the modified tower, each tower section is shortened by 1 m, while the top and bottom diameters are kept unchanged. This design is flawed and, when considering a rigid hull, results in a tower natural frequency of 0.399 Hz, which is within the 3P range. Resonance

TABLE 2 Floating wind turbine (FWT) characteristics

Parameter	Semi	Spar	TLP
Water depth, m	130	320	200
Draft, m	18.3	120.0	35.3
Displacement, tonnes	9280	13 350	17 360
Platform pitch inertia about SWL, kgm ²	4.66×10^9	6.53×10^9	1.49×10^8
Platform yaw inertia about SWL, kgm ²	7.12×10^9	2.49×10^8	1.30×10^9

Abbreviations: SWL, still water line; TLP, tension leg platform.

TABLE 3 FWT mooring properties

Parameter	Semi	Spar	TLP
Number of lines (–)	4	3	3
Radius to anchors, m	793.5	849.5	39.6
Unstretched mooring line length, m	833.24	902.20	164.67
Equivalent mooring line mass density, kg/m	188.2	233.1	5737.0
Equivalent mooring line axial stiffness, N	8.035×10^8	384.243×10^6	1.557×10^{11}
Fairlead depth below SWL, m	6.333	70	35.3
Additional yaw spring stiffness, Nm/rad	0	1.47×10^8	0
Pretension, kN	610	2600	28 000

Abbreviations: SWL, still water line; TLP, tension leg platform.

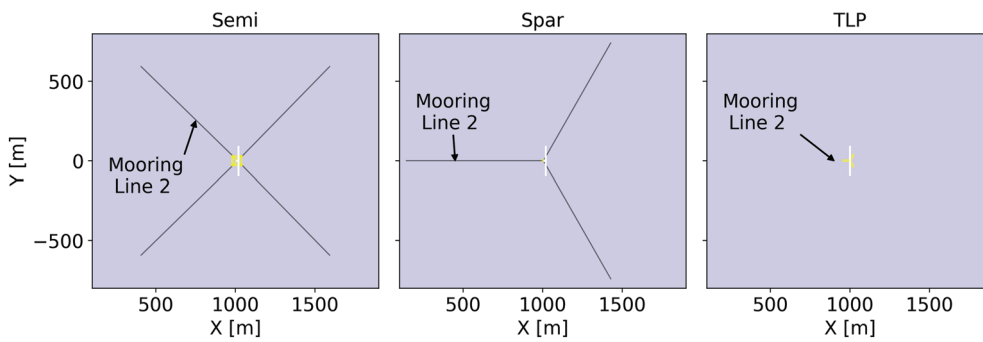


FIGURE 3 Mooring layout for the the semi (left), spar (middle), and tension leg platform (TLP) (right). The TLP mooring lines are vertical and therefore not visible. Fatigue results are only presented for a single line (mooring line 2) for each concept [Colour figure can be viewed at wileyonlinelibrary.com]

of the tower natural frequency with 3P excitation can result in increased fatigue loading. A more representative tower would require redesign to move the natural frequency above or below the 3P range, including consideration of hull flexibility.⁴²

2.2.3 | TLP platform

The TLP used in this study is the NTNU 10-MW TLP but with a slightly modified hull. The design is based on a 5-MW platform, TLP#3 from Bachynski,⁴³ with three steel pipe tendons connected to pontoons. This design is very stiff in heave, roll, and pitch, resulting in coupling between the tower bending and pitch natural frequencies. The original hull design has one large central column with a freeboard of 10 m, requiring a shortened tower. Preliminary calculations showed that shortening the tower resulted in a tower/pitch natural frequency close to the lower end of the 3P range. To decrease the tower/pitch frequency, the connection between the platform and tower was softened. The freeboard was removed, and a taper from the tower base diameter to the original diameter 10 m below the SWL was introduced, decreasing the tower/pitch frequency from 0.287 to 0.251 Hz. The tower/pitch frequency along with other important natural frequencies can be found in Table 7.

3 | DYNAMIC ANALYSIS

3.1 | Environmental conditions

The environmental conditions (ECs) are derived from a deep-water (200 m) reference site⁴⁴ in the North Sea (Site 14). Hindcast data of 1-hour averaged wind and sea states are used to generate 10-year wind and wave statistics. Even though each platform is designed for a different water depth, the same environmental conditions are applied. A summary of the ECs can be found in Table 8.

Three wind speeds and two turbulence levels were chosen for the dynamic analysis (the second turbulence level is examined only for one FWT concept, the semi). The three wind speeds of 8, 11.4, and 16 m/s, denoted herein as below, rated, and above, respectively, were chosen to investigate how meandering changes with wind speed in the different regimes of turbine operation with respect to the rated speed and because

TABLE 4 Wind turbine controller characteristics

Parameter	Onshore	Semi	Spar	TLP
Blade pitch controller natural frequency, Hz	0.06	0.01	0.02	0.06
Blade pitch K_t , rad/(rad/s)	0.141 233	0.041 415	0.015 693	0.141 233
Blade pitch K_p , rad/rad	0.524 485	0.208 004	0.174 828	0.524 485
Above-rated strategy	Constant power	Constant torque	Constant torque	Constant power

Abbreviation: TLP, tension leg platform.

Degree of Freedom	OpenFAST, s	OpenFAST, Hz
Surge	117.6	0.009
Heave	19.3	0.052
Pitch	29.4	0.034
Yaw	93.5	0.011
Tower	1.9	0.526

TABLE 5 Lifes50+ Nautilus 10-MW semisubmersible natural periods and frequencies in OpenFAST³⁵

Degree of Freedom	SIMa, s	OpenFAST, s	SIMa, Hz	OpenFAST, Hz
Surge	103.3	102.4	0.010	0.010
Heave	31.3	31.3	0.032	0.032
Pitch	35.5	35.1	0.028	0.029
Yaw	7.6	8.1	0.016	0.017
Tower	2.4	2.5	0.417	0.399

TABLE 6 NTNU 10-MW spar natural periods and frequencies in SIMa and OpenFAST

TABLE 7 NTNU TLP 10-MW natural periods and frequencies in SIMA and OpenFAST

Degree of Freedom	SIMA, s	OpenFAST, s	SIMA, Hz	OpenFAST, Hz
Surge	45.53	43.40	0.022	0.023
Heave	0.55	0.54	1.818	1.868
Yaw	20.87	20.48	0.048	0.049
Tower/pitch	3.49	3.98	0.287	0.251

TABLE 8 Environmental conditions

u_{hub} , m/s	TI _{hub,high} , %	TI _{hub,low} , %	α (-)	H_s , m	T_p , s
8.0	17.40	8.00	0.14	2.3	8.3
11.4	14.89	6.00	0.14	2.9	8.4
16.0	13.20	7.00	0.14	3.5	8.6

they demonstrate different FWT dynamic responses. At 8 and 16 m/s, the DTU 10 MW operates with approximately equivalent thrust. Because of the low temporal resolution of the hindcast data, no information regarding turbulence can be deduced. The higher of the two turbulence levels follows the specification for a Class C site in the IEC standard¹²:

$$\sigma_u = I_{ref}(0.75u_{hub} + b); \quad b = 5.6 \text{ m/s}, \quad (1)$$

where σ_u is the characteristic standard deviation of the wind speed in the longitudinal direction, u_{hub} is the hub-height wind speed, and I_{ref} is a reference value of 0.12. The lower turbulence level is a characteristic of offshore conditions and varies little with mean wind speed.⁴⁵ The shear exponent $\alpha = 0.14$ is also specified by the IEC standard and is a characteristic for neutral atmospheric stability conditions.

For each EC, six wind fields were generated. Only one realization of waves corresponding to each wind speed is used so that differences in responses can be purely attributed to changes in the wind field. Additionally, FWT1 and FWT2 see the same time domain long-crested wave realization, and the wind and waves have the same heading. The significant wave height (H_s) and peak period (T_p) are chosen as the most probable values for aligned wind and waves for the given wind speeds, based on the joint probability distribution for the reference site.

3.2 | Turbulence models

The wind fields are generated using the Kaimal model in NREL's TurbSim⁴⁶ and the Mann turbulence model in the IEC 64 bit turbulence generator.⁴⁷ While the frequency content should be similar (following the Kaimal spectrum), the numerical methods with which the wind fields are synthesized differ considerably. The Mann model uses a spectral tensor derived from the conservation of momentum and mass to generate turbulence under neutral atmospheric conditions. The model has three parameters that can be used to fit it to a given wind spectrum and turbulence intensity: an energy dissipation rate parameter $\alpha\varepsilon^{2/3}$, a shear distortion parameter Γ , and a length scale describing the size of energy-containing eddies L . The Kaimal model also assumes neutral atmospheric conditions; however, the time-varying wind in TurbSim is synthesized using an inverse Fourier transform with an empirically fit exponential coherence model, then superimposed onto the mean profile. In the Kaimal model, time-dependent wind is generated in 2D planes, whereas the Mann model generates static wind in a 3D volume. Taylor's hypothesis is used to extend to a third dimension in both cases.

3.2.1 | Spatial coherence

Spatial coherence is defined as the correlation in energy content between two spatially separated time series. Regarding wind fields, the two time series are spatially separated in either the lateral or vertical direction. The magnitude-squared coherence as a function of frequency is formulated as:

$$Coh_{ijk}(f) = \frac{|C_{ij}(f)|^2}{P_i(f)P_j(f)}, \quad (2)$$

where f is frequency; P_i and P_j are the power spectra of each individual time series; C_{ij} is the cross spectrum between those two time series; and $K = u, v$, or w refers to the specific velocity component. Note that coherence will only be calculated for single velocity components as cross coherence is not examined within the scope of the present work and that magnitude-squared coherence and coherence are used interchangeably hereinafter.

Within the Kaimal turbulence model, coherence is added to independently generated points using an exponential function based on empirical formulations. This formulation is defined as:

$$Coh_{ijk}(\delta, f) = \left[\exp \left(-a_k \sqrt{\left(\frac{f\delta}{u_{hub}} \right)^2 + (\delta b_k)^2} \right) \right]^2, \quad (3)$$

where δ is the separation distance between time-series i and j , a_k is the coherence decrement parameter, and b_k is the coherence offset parameter. In the IEC standard,¹² the coherence model is only applied to the u -velocity component.

Model Name	$a_u (-)$	$b_u (\text{m}^{-1})$	$a_v (-)$	$b_v (\text{m}^{-1})$	$a_w (-)$	$b_w (\text{m}^{-1})$
Kaimal-Coh u	12.0	3.5273×10^{-4}	∞	0.0	∞	0.0
Kaimal-Coh all	12.0	3.5273×10^{-4}	12.0	3.5273×10^{-4}	12.0	3.5273×10^{-4}

TABLE 9 Spatial coherence parameters specified in TurbSim

Coherence is inherent to the Mann model and given by the integral of the spectral tensor, ϕ_{ij} , as a function of the nondimensional separation distance and the spatial wave number:

$$\text{Coh}_{ijk}(k, \delta) = \frac{\left| \int \int \phi_{ij} dk_y dk_z e^{-ik_y \delta_y} e^{-ik_z \delta_z} dk_y dk_z \right|^2}{\int \int \phi_{ij} dk_y dk_z \int \int \phi_{jj} dk_y dk_z}, \quad (4)$$

where δ_y and δ_z are the separation distances of the two points in the lateral and vertical directions and k_y and k_z are the spatial wave numbers corresponding to the lateral and vertical directions. There is no analytical solution to this formulation, and the coherence is computed using numerical methods.

3.2.2 | Ambient wind generation

Since the IEC standard does not provide values of a_K and b_K for the lateral and vertical velocity components, in TurbSim, the default coherence parameters within the Kaimal turbulence model for a_v , a_w , b_v , and b_w (listed in Table 9) result in no spatial coherence. Previous work has found that the default parameters a_K , b_K in TurbSim result in negligible lateral wake meandering.^{28,29} While using the default parameters in TurbSim does not provide realistic wake meandering behavior, the model is included here as the first of the two methods using the Kaimal turbulence model because the result is an approximately uniform, axial wake deficit. The results from this method, denoted “Kaimal-Coh u ,” help to isolate the wake effects specifically related to meandering.

To induce meandering in the second method, we specify values for a_K and b_K (found in Table 9). The selected values for the second model, referred to as “Kaimal-Coh all,” are the same as those for the longitudinal component in the first method. The selected values have been shown to match meandering from LES reasonably well.²⁸ Although previous work has found the lateral and vertical coherence to differ compared with the longitudinal coherence,^{48,49} defining more precise coherence parameters would require a separate analysis and is left for future work.

The third method, referred to as “Mann,” uses the Mann turbulence model. In the present work, the reading of the Mann wind field in FAST.Farm has been reversed in the longitudinal direction. Discussion of this decision can be found in Appendix A.

The three wind fields have the width and height of the low-resolution domain and have identical spatial grids discretized in accordance to the high-resolution domain surrounding each individual turbine: $\Delta Y = \Delta Z = 7.5$ m and a time step, dt , of 0.125 second. The wind fields propagate in the positive x -direction at the wind speed of a reference height at the vertical midpoint of the domain, defined schematically in Figure 4 (note that in FAST.Farm, the vertical domain extends well above the top of the rotor to account for vertical meandering). The wind speed at the reference height, u_{ref} , is calculated using the wind profile power law. Converting between time and space results in a spatial resolution in the longitudinal dimension that depends on the wind speed:

$$u_{ref} = u_{hub} \left(\frac{z_{ref}}{z_{hub}} \right)^{\alpha}, \quad (5)$$

$$\Delta X = dt u_{ref}, \quad (6)$$

where z_{hub} is the hub height; z_{ref} is the reference height; u_{hub} is the wind speed at hub height; and u_{ref} is the wind speed at the reference height.

3.3 | Fatigue calculations

The IEC standard for offshore wind turbines recommends six simulations of 10 minutes in duration or a continuous 1-hour simulation.³⁰ Six 1-hour simulations (after a 400-second transient) are used to capture the effects of the long natural periods and the stochastic variation in the

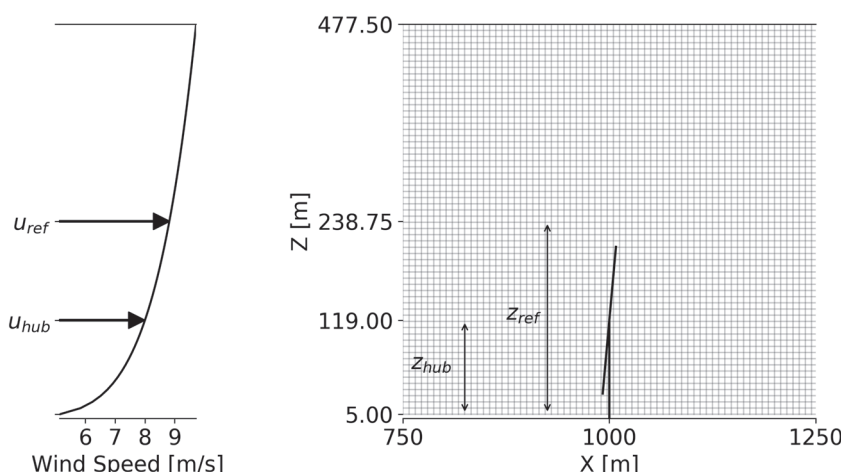


FIGURE 4 Wind field discretization for the scenario with a wind speed of 8 m/s. Note that the vertical domain begins at $z = 5$ m since surface layer processes are not included in the spectral models

results. Fatigue loading is assessed using short-term damage-equivalent loads (DELs) calculated using NREL's MLife.⁵⁰ DELs transform irregular loads into a constant-amplitude constant-frequency fatigue load that produces equivalent damage:

$$D_j^{ST} = \sum_i \frac{n_{ji}}{N_{ji}} = \frac{n_j^{STeq}}{N_j^{eq}}, \quad (7)$$

where D_j^{ST} is the short-term accumulated fatigue damage from time-series j , n_{ji} is the i th cycle count, N_{ji} is the number of cycles to failure, n_j^{STeq} is the total equivalent fatigue counts, and N_j^{eq} is the equivalent number of cycles until failure. The formulation for the short-term DELs, DEL_j^{ST} , applied here is as follows:

$$DEL_j^{ST} = \left(\frac{\sum_i (n_{ji}(L_{ji}^R)^m)}{n_j^{STeq}} \right)^{\frac{1}{m}}, \quad (8)$$

where f^{eq} is the DEL frequency taken as 1 Hz, T_j is the elapsed time, m is the Wöhler exponent taken as 3 for the steel tower and mooring lines and 10 for the composite blades, and L_{ji}^R is the cycle's load range without using the Goodman correction.

4 | RESULTS AND DISCUSSION

4.1 | Wind fields

The three wind field generation methods used in the FAST.Farm simulations have important consequences for platform responses. The power spectral density (PSD) of the three wind velocity components at the hub height is shown in Figure 5. Only the below and above-rated wind speed scenarios for TI_{high} are shown, as trends were identical for the other cases. Across all three velocity components, the difference in energy content between the first two methods was negligible. For the u - and w -velocity components, the PSDs for the Mann and Kaimal turbulence models match very well, although the Mann model had less energy content at higher frequencies (greater than 1 Hz). Additionally, the Mann model had less energy at lower frequencies in the v -velocity component.

The low-frequency coherence between lateral separation distances (δ_y) at the hub height in the three velocity components is shown in Figures 6 and 7. Coherence was calculated for three lateral separation distances as a function of rotor diameter: $\delta_y \approx D/20$, $D/5$, and $D/2$, respectively. The distances were approximate because the time series used for numerically calculating the coherence were at exact grid points within the wind fields. As expected, the first two wind field generation methods had identical coherence for the u -velocity component. For the small separation distance, Mann had less coherence in u and w but greater coherence in v compared with Kaimal-Coh all. At large and intermediate distances, Kaimal-Coh all generally had greater coherence in all three of the velocity components. In Figure 8, the lateral component of the wind field shows slightly larger eddies in Kaimal-Coh all compared with Mann, which is consistent with larger coherence for Kaimal-Coh all at intermediate to large separation distances.

FIGURE 5 Power spectral density of the longitudinal (left), lateral (middle), and vertical (right) velocity components for each inflow method (only TI_{high}) [Colour figure can be viewed at wileyonlinelibrary.com]

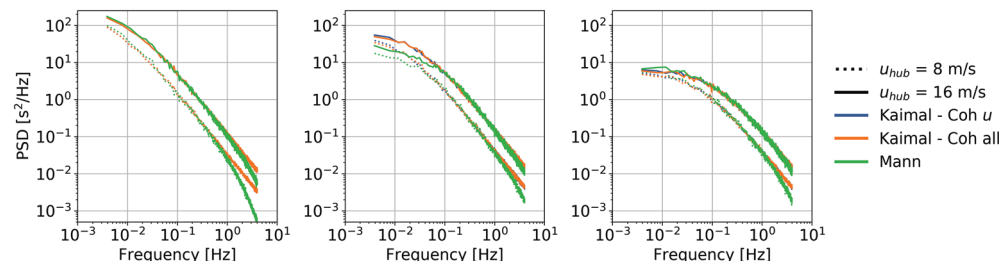
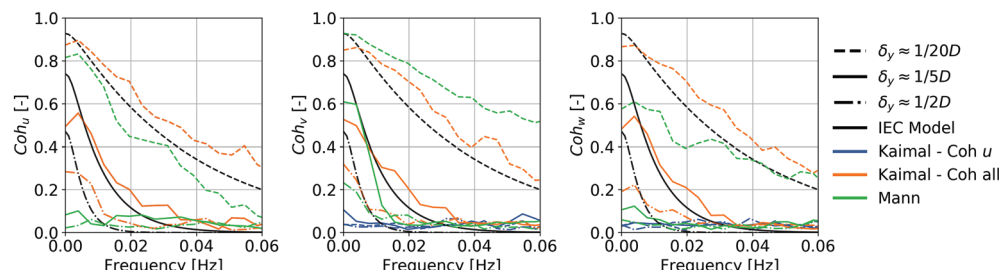


FIGURE 6 Coherence between two points $(0, z_{hub})$ and (δ_y, z_{hub}) in the u -, v -, and w -velocity components for each inflow method in the below-rated wind speed scenario averaged over six seeds. IEC model corresponds to Equation (3) using the Kaimal-Coh all coherence parameters [Colour figure can be viewed at wileyonlinelibrary.com]



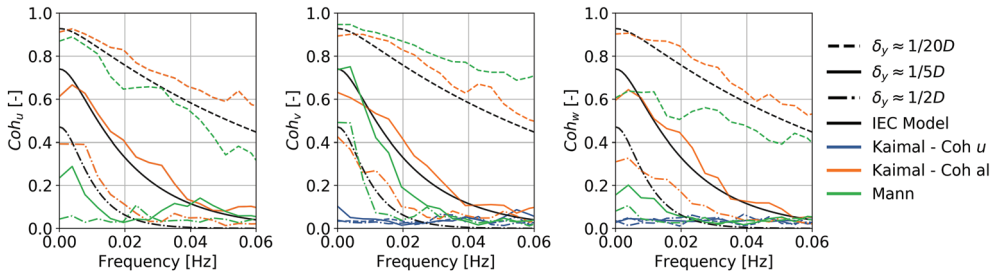


FIGURE 7 Coherence between two points $(0, z_{hub})$ and (δ_y, z_{hub}) in the u -, v -, and w -velocity components for each inflow method in the above-rated wind speed scenario averaged over six seeds. IEC model corresponds to Equation (3) using the Kaimal-Coh all coherence parameters [Colour figure can be viewed at wileyonlinelibrary.com]

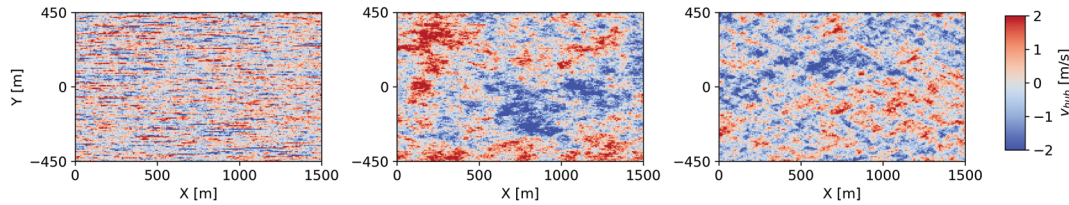


FIGURE 8 Example instantaneous flow visualization of the v -velocity component at hub height for Kaimal-Coh u (left); Kaimal-Coh all (middle); and Mann (right). The domain of the wind fields has been truncated for visualization [Colour figure can be viewed at wileyonlinelibrary.com]

4.2 | Wake meandering and flow visualizations

Figure 9 shows the lateral meandering behavior (wake center position) of the three inflow methods for the below, rated, and above wind speed scenarios with high TI. Results for the semi are shown; the differences in lateral meandering between the three platforms were negligible. As expected, Kaimal-Coh u , the inflow method without coherence in the lateral and vertical velocity components, resulted in a uniform wake deficit without meandering. Regarding the two inflow methods with meandering, there were two clear observations: wake meandering decreased with increasing wind speed but occurred at slightly higher frequencies and, compared with Mann, Kaimal-Coh all resulted in slightly more meandering at higher frequencies than Mann. For the below wind speed scenario, the scenario with the most extreme meandering, the standard deviation of the lateral wake center position for Kaimal-Coh all was $0.48D$ compared to $0.35D$ for Mann. As discussed in Section 4.1, the lateral velocity component in Kaimal-Coh all had greater energy content and greater coherence for intermediate and large lateral separation distances at lower frequencies. An instantaneous flow visualization of the hub-height wind speed in the horizontal plane is shown in Figure 10. While the flow fields for the first two methods look nearly identical, the differences in spatial coherence clearly influenced the wake centers.

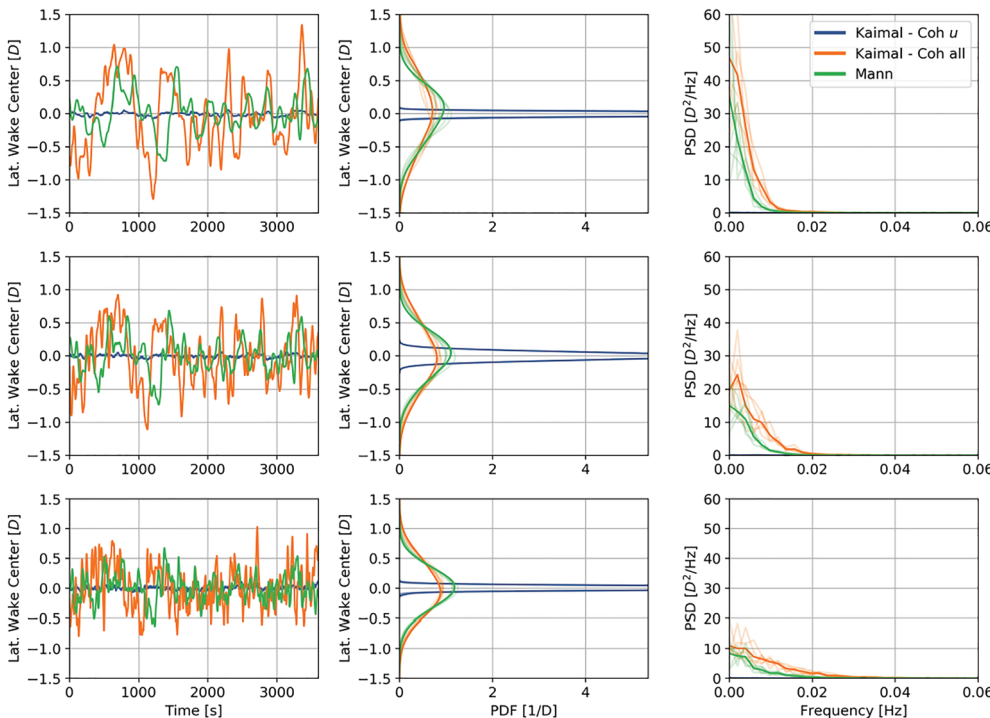


FIGURE 9 Time series for a single simulation (left), probability density function (PDF) (middle), and power spectral density (PSD) (right) for six simulations of FWT1's lateral wake center position at $8D$ for the below (top), rated (middle), and above (bottom) wind speed scenarios. For the PDF and PSD plots, the average of the six simulations is the darker line [Colour figure can be viewed at wileyonlinelibrary.com]

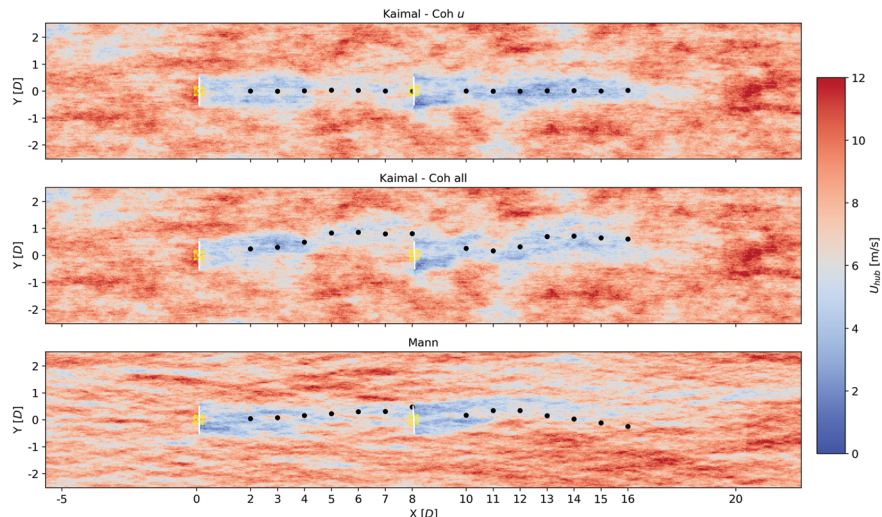


FIGURE 10 Instantaneous flow visualization of the hub-height wind speed modulus for each inflow method [Colour figure can be viewed at wileyonlinelibrary.com]

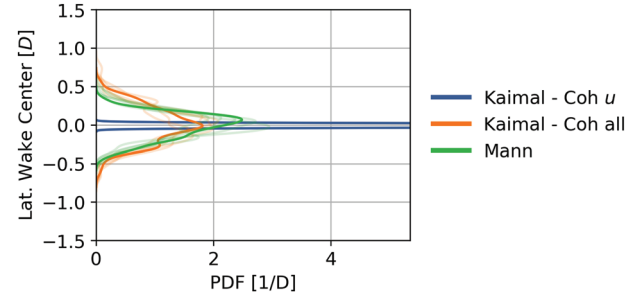


FIGURE 11 Probability density function (PDF) of FWT1's lateral wake center position at 8D for the below-rated, low TI wind speed scenario. The average of the six simulations is the darker line [Colour figure can be viewed at wileyonlinelibrary.com]

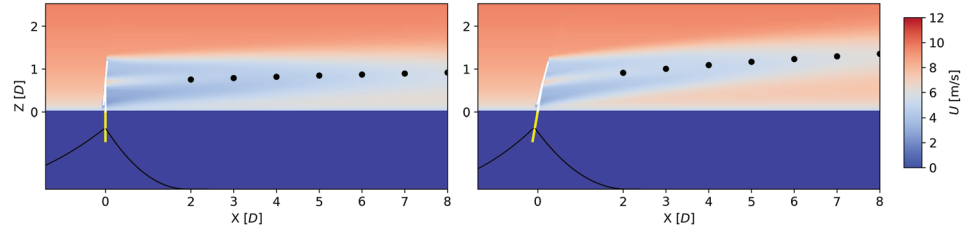


FIGURE 12 Flow visualization of the wind speed in the XZ-plane for a spar without (left) and with (right) a pitch offset of 10°. The black dots represent the vertical wake center position [Colour figure can be viewed at wileyonlinelibrary.com]

There was decreased meandering in the low TI case compared with the high TI case, but the same trends were observed. Figure 11 shows the PDF of FWT1's lateral wake center position at 8D for the low TI case (only the below rated wind speed scenario is shown). For the low TI case, the differences between Kaimal-Coh all and Mann were less pronounced. In the below wind speed scenario, the standard deviations in the wake center at 8D were 0.23D for Kaimal-Coh all and 0.18D for Mann.

While differences in lateral meandering between the three platforms were negligible, vertical meandering differed (Figure 12). The heave motions are so small (standard deviations less than 0.5 m) relative to the size of the rotor that any differences in vertical meandering can likely be attributed to pitch motions. During operation for the below-rated wind speed scenario, the mean platform pitch positions for the semi, spar, and TLP were approximately 1°, 4°, and 0°, respectively. Regardless of inflow method, a greater mean platform pitch resulted in the wake deflecting to a higher vertical location. It is difficult to identify a clear relationship between vertical meandering and motions, but qualitatively, platforms that pitch more have a greater spread in their vertical wake center position.

Vertical wake deflection was explored further using steady wind with shear ($u_{hub} = 8 \text{ m/s}$) in FAST.Farm. Figure 13 shows the flow fields in the vertical plane for a FAST.Farm simulation of a spar with a fixed pitch of 0° and 10°. The vertical wake center 8D downstream for the spar without pitch deflected 0.25D above hub height while the pitched spar's wake deflected 0.68D above hub height. The vertical wake deflection for the spar without pitch was primarily due to shaft tilt. The combination of the shaft tilt and platform pitch is analogous to the yaw angle used in lateral wake deflection formulations for wake steering wind farm control.^{19,51} In principle, vertical wake deflection for FWTs could be controlled using active ballasting, blade pitch control, mooring line tension, or other methods.

Vertical wake deflection is important to consider because it affects the velocity deficit downstream. Hereinafter, the velocity deficit is defined as:

$$\bar{u}_{hub_{FWT1}} - \bar{u}_{hub_{FWT2}}, \quad (9)$$

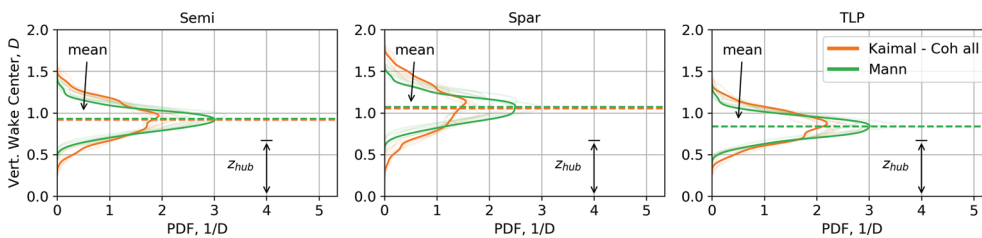


FIGURE 13 Probability density function (PDF) of FWT1's vertical wake center position at 8D for the below-rated wind speed scenario. Dashed lines are placed at the mean vertical wake center position [Colour figure can be viewed at [wileyonlinelibrary.com](#)]

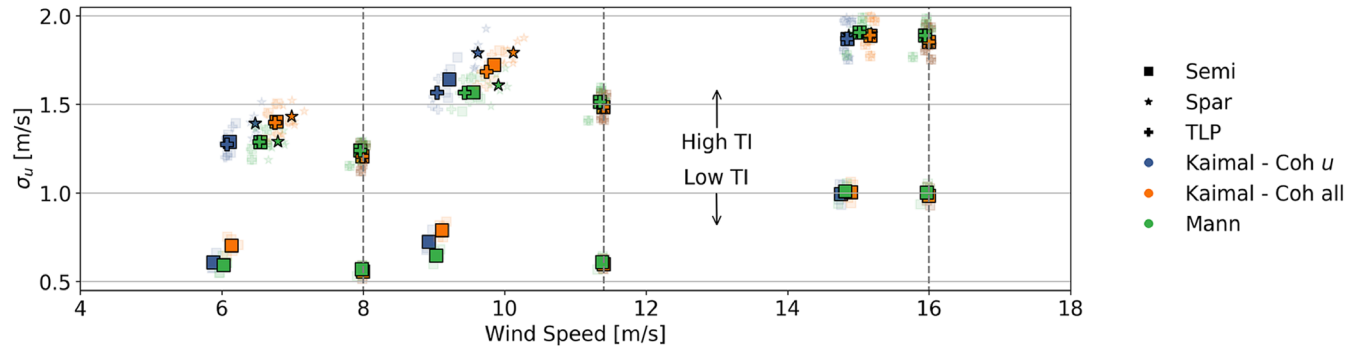


FIGURE 14 Wind speed standard deviation, $\sigma_{u_{hub}}$, as a function of mean hub-height wind speed, i.e., the corresponding $\sigma_{u_{hub}}$ for FWT1 is plotted at the free stream wind speed ($\bar{u}_{hub} \approx 8, 11.4, 16$ m/s) while the corresponding $\sigma_{u_{hub}}$ for FWT2 is plotted at the waked wind speed ($\bar{u}_{hub} < 8, 11.4, 16$ m/s). Each point represents the average value from each of the six simulations. The individual value from each simulation are still visible as transparent points [Colour figure can be viewed at [wileyonlinelibrary.com](#)]

where $\bar{u}_{hub_{FWT1}}$ and $\bar{u}_{hub_{FWT2}}$ are the mean wind speeds at hub height for FWT1 and FWT2. The velocity deficit is relevant for fatigue since certain load effects depend on the rotor speed and subsequent harmonics. Additionally, the behavior of low-frequency motions (and subsequent loading) for FWTS can vary significantly with incoming wind speed.

Figure 14 shows the hub-height wind speed standard deviation as a function of mean incoming wind speed \bar{u}_{hub} ; ie, the corresponding $\sigma_{u_{hub}}$ for FWT1 is plotted at the ambient wind speed ($\bar{u}_{hub} \approx 8, 11.4, 16$ m/s) while the corresponding $\sigma_{u_{hub}}$ for FWT2 is plotted at the waked wind speed ($\bar{u}_{hub} < 8, 11.4, 16$ m/s). Because an even number of grid points is used in the wind fields, there is no grid point exactly at the hub; therefore, due to interpolation, $\sigma_{u_{hub}}$ for FWT1 is slightly smaller than the prescribed value. The characteristic standard deviation always increased for the downstream turbine. Differences in the increase of $\sigma_{u_{hub}}$ were correlated with the amount of meandering induced by the inflow method and the velocity deficit. This created “apparent” turbulence, which has been described by Madsen et al.¹⁴

The x-coordinate of the standard deviations shown in Figure 14 provides information about the velocity deficit. Regardless of inflow method, compared with the semi and TLP, the spar had a smaller velocity deficit due to vertical wake deflection. A few other trends and observations in Figure 14 are important to note. The velocity deficit was greatest for Kaimal-Coh u and smallest for Kaimal-Coh all. Intuitively, the velocity deficit depends on meandering: More meandering meant a smaller velocity deficit. Furthermore, the velocity deficit in the low turbulence case was always greater than the velocity deficit in the high turbulence case.

4.3 | Platform motions

Figure 15 shows the platform surge, pitch, and yaw motion standard deviations of FWT1 and FWT2 for all three platforms as a function of \bar{u}_{hub} . For the TLP, the surge and yaw standard deviations are magnified by a factor of 4, and the pitch standard deviations are magnified by a factor of 400 for visualization. For the semi, only motions for the high turbulence case are shown, as the behavior in the low turbulence case showed similar trends. In addition to the FAST.Farm results, Figure 15 includes single turbine simulations of the semi using OpenFAST for the three wind speed scenarios with σ_u held constant, but the ambient wind speed decreased uniformly by 2 and 4 m/s. The same wave realizations are used in the OpenFAST and in FAST.Farm simulations despite the decrease in mean wind speed.

Consistent with previous research, the Mann turbulence model resulted in smaller surge and pitch motions but greater yaw motions compared with the Kaimal turbulence model for all three FWT concepts. Bachynski and Eliassen²⁴ provide a more comprehensive discussion regarding the dynamics of large FWTS when using the Mann or Kaimal turbulence models. For the semi and spar, surge, pitch, and yaw motions were dominated by low-frequency responses. For the TLP, surge and yaw motions were similarly dominated by low-frequency responses; however, pitch motions due to linear wave loads and at the tower frequency were also important.

Low-frequency surge and pitch spectra for the semi can be found in Figures 16 and 17. For the below wind speed scenario, surge responses were mostly quasi-static while resonant responses at the surge natural frequency dominated for the rated and above scenarios. Additionally, resonant

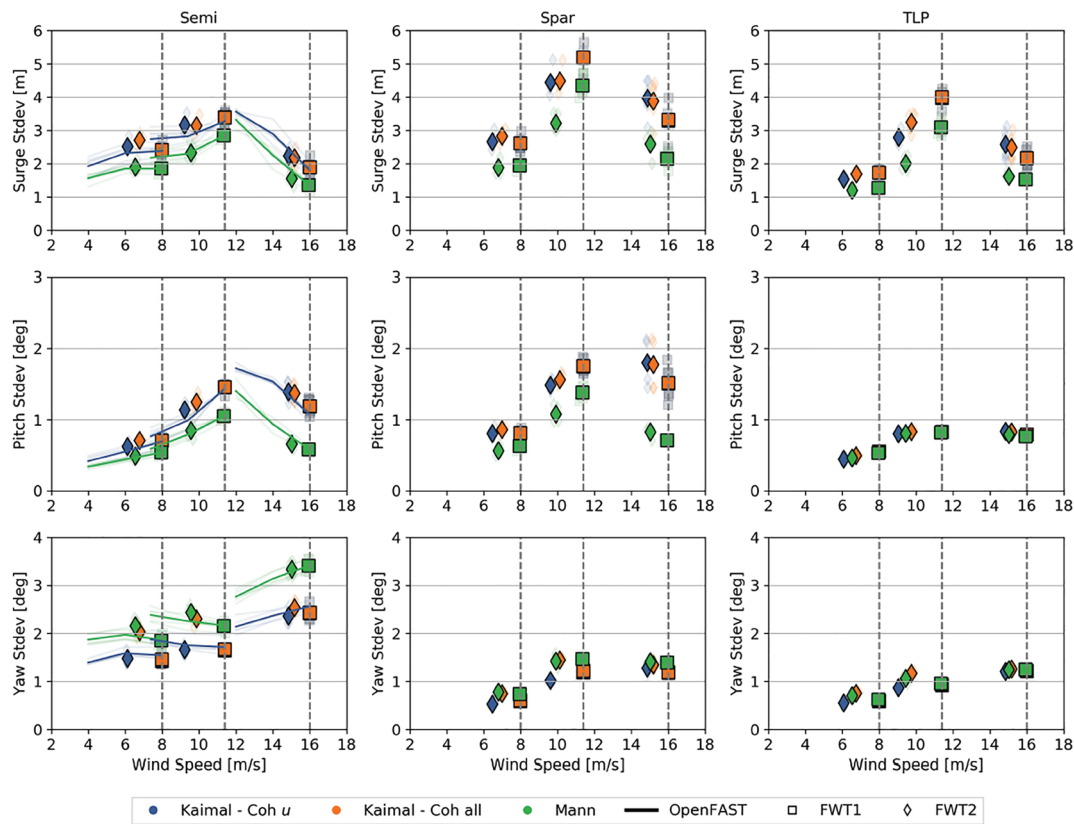


FIGURE 15 Standard deviations of platform surge (top), pitch (middle), and yaw (bottom) motions for FWT1 and FWT2 as a function of \bar{u}_{hub} . The dark points and lines are the average of the six simulations while the lighter points and lines are the results from individual simulations. For the TLP, the surge and yaw standard deviations are magnified by a factor of 4 and the pitch standard deviations are magnified by a factor of 400 [Colour figure can be viewed at wileyonlinelibrary.com]

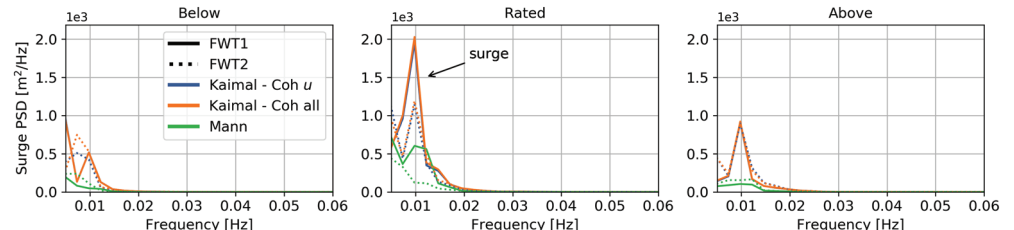


FIGURE 16 Low-frequency surge response of the semi for each wind speed scenario [Colour figure can be viewed at wileyonlinelibrary.com]

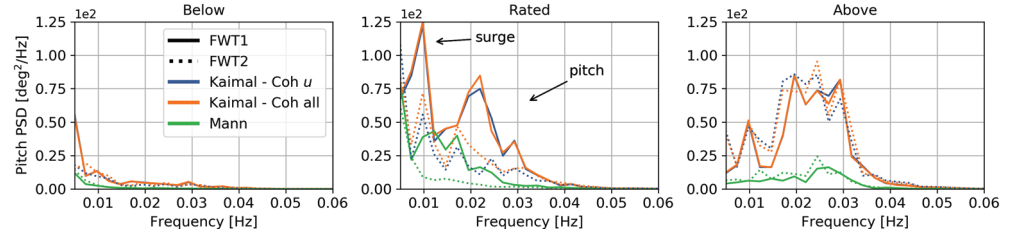


FIGURE 17 Low-frequency pitch response of the semi for each wind speed scenario [Colour figure can be viewed at wileyonlinelibrary.com]

response at the surge natural frequency was greatest for the rated scenario, when the turbine operated with the greatest thrust. Pitch responses followed a similar trend. Decreased low-frequency energy content for Mann compared with Kaimal-Coh *u* and Kaimal-Coh *all* was also apparent.

Yaw responses were similarly dominated by low-frequency motions. Figure 18 shows that the semi responded primarily at its natural frequency and, along with Figure 15, illustrates that low-frequency yaw motion increased with increasing wind speed. Low-frequency yaw motion was greater for Mann compared with Kaimal-Coh *u* and Kaimal-Coh *all*.

The trends in the responses were similar for the other two platforms, although the surge and pitch natural frequencies differ significantly.

The effect of wake meandering on surge and pitch motions is secondary. Figures 16 and 17 reveal that differences in the low-frequency surge and pitch responses for FWT2 and FWT1, whether the turbine responded quasi-statically or at the surge and pitch natural frequencies, were a function of the incoming wind speed. The results from the OpenFAST simulations in Figure 15 confirmed that the standard deviations of the

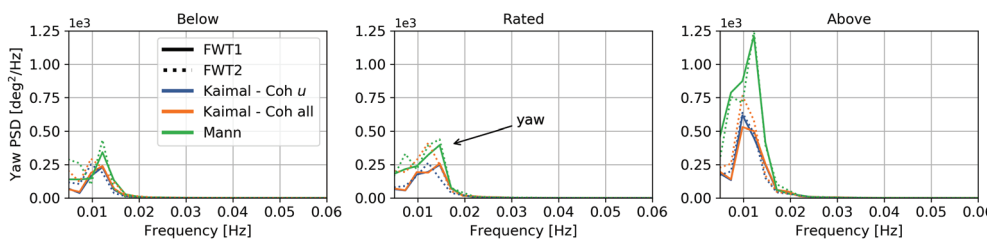


FIGURE 18 Low-frequency yaw response of the semi for each wind speed scenario [Colour figure can be viewed at wileyonlinelibrary.com]

in-plane motions in FAST.Farm could largely be attributed to the velocity deficit with some small differences because the velocity deficit induced by the wake in FAST.Farm is not uniform over the rotor.

However, the OpenFAST simulations demonstrated the significant influence of wake meandering on yaw motions. For the inflows that induced meandering, Kaimal-Coh all and Mann, the yaw motions of FWT2 were significantly higher than those of the OpenFAST simulations. This can be attributed to increased low-frequency response for FWT2 compared with FWT1, as seen for the semi in Figure 18. For the below and rated scenarios, comparing FWT2 for Kaimal-Coh u and Kaimal-Coh all shows that wake meandering resulted in greater response at the yaw natural frequency and lower (less than 0.02 Hz) frequencies. For the below and rated wind speed scenarios, yaw motion standard deviations for the semi increased by close to 40% for FWT2 compared with FWT1 (although not shown, yaw motion standard deviations for the semi increased by a factor of 2 for FWT2 compared with FWT1 in the TI_{low} case). While the semi is the only FWT concept with a very low natural frequency in yaw, increased quasi-static low-frequency response for the spar and TLP was also observed. Yaw motion standard deviations for the spar and TLP increased on the order of 20% for FWT2 compared with FWT1. For the above-rated scenario, the changes in yaw motion standard deviations were small (approximately 5% for the semi and approximately 1% for the spar and TLP).

4.4 | Structural loading

Fatigue due to four global load effects, the tension of mooring line 2 (labeled in Figure 3), the tower base fore-aft bending moment (TBFABM), the tower top yaw moment (TTYM), and the blade root out-of-plane moment (BROoPM), was examined.

The main interest of the work presented in this paper is how the structural loading for a waked FWT (FWT2) compares with that of an FWT operating in free-stream conditions (FWT1). Therefore, in this subsection, we quantify the difference in fatigue loading for each FWT concept as follows:

$$\text{Percent Difference} = \frac{\text{DEL}_{\text{FWT2}} - \text{DEL}_{\text{FWT1}}}{\text{DEL}_{\text{FWT1}}} \times 100. \quad (10)$$

Figure 19 shows the percent differences in DELs for the tower base fore-aft bending moment of all three FWT concepts in each wind speed scenario. For the rated scenario, fatigue loading in the tower base fore-aft bending moment decreased regardless of FWT concept. Fatigue

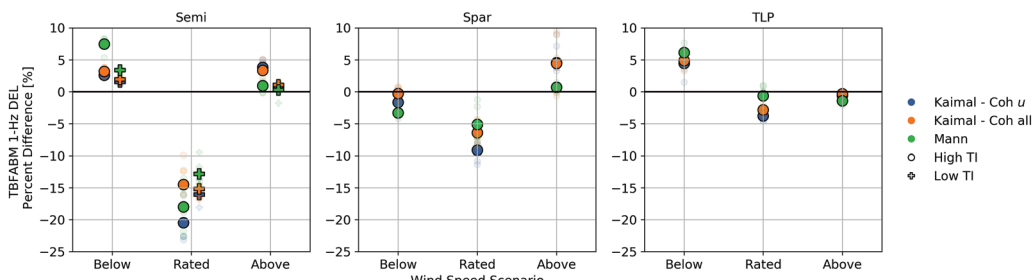


FIGURE 19 Tower base fore-aft bending moment percent difference in damage-equivalent load (DEL) between FWT1 and FWT2 for each wind speed scenario [Colour figure can be viewed at wileyonlinelibrary.com]

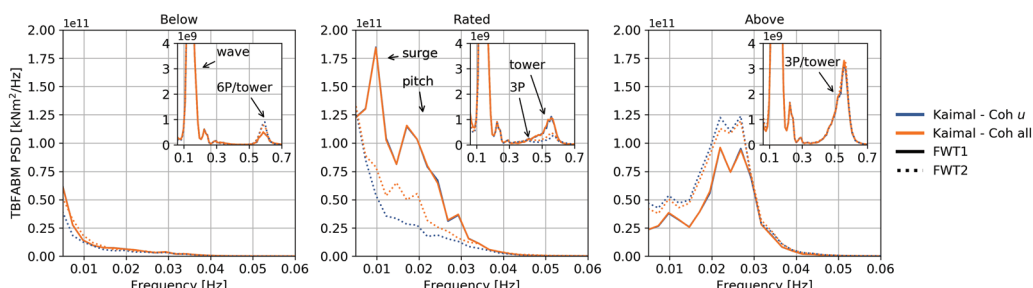


FIGURE 20 Tower base fore-aft bending moment spectra of FWT1 and FWT2 for the semi in each wind speed scenario. Higher frequency responses are shown as an inset with a smaller vertical scale [Colour figure can be viewed at wileyonlinelibrary.com]

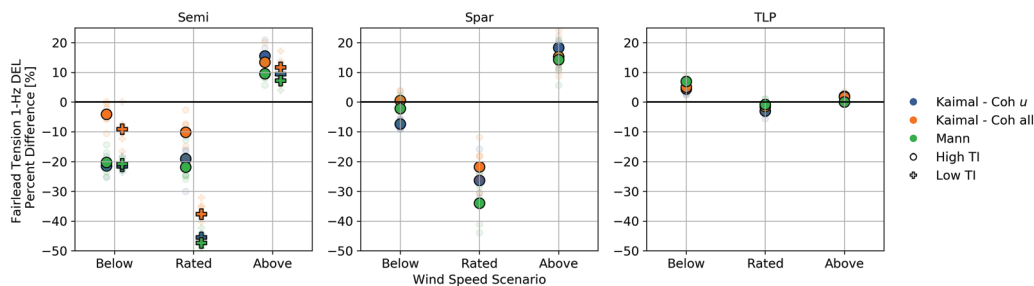


FIGURE 21 Mooring line 2 tension percent difference in damage-equivalent load (DEL) between FWT1 and FWT2 for each wind speed scenario [Colour figure can be viewed at wileyonlinelibrary.com]

loading increased in the semi and TLP for the below scenario but decreased for the spar. For the above scenario, fatigue loading increased for the semi and spar but decreased for the TLP. Specific differences between the three concepts could largely be attributed to the tower natural frequency in each design. In general, these trends were not sensitive to inflow method nor turbulence level.

Figure 20 shows the tower base fore-aft bending moment spectra for the semi. Low-frequency motions translated to low-frequency structural loading but load responses at higher frequencies, such as the rotor frequency (1P) and blade-passing frequency (3P), while usually small compared with low frequencies, significantly influenced short-term DELs due to their high cycle count. Only responses for the semi are shown as similar trends were observed in the other three FWT concepts. Additionally, only Kaimal-Coh *u* and Kaimal-Coh *all* are compared with directly address the effect of meandering on structural loading. Low-frequency loading was largely correlated with the pitch response, indicating that the velocity deficit was more influential than meandering itself. As shown most clearly for the rated scenario, the low-frequency loading of FWT2 for Kaimal-Coh *u* was more quasi-static compared with Kaimal-Coh *all* since Kaimal-Coh *u* had a greater velocity deficit. In addition to low-frequency responses, there were higher frequency responses from waves and responses at the tower natural frequency. At frequencies above the wave spectra, differences between the three wind speed scenarios were due to shifts in the 3P and 6P excitations. The fatigue loading increased for the below rated scenario because the lower 6P excitation resulted in some resonant responses at the tower frequency. FWT2 in the rated scenario saw a more broadband 3P excitation resulting in less resonant response at the tower frequency, which reduced fatigue loading. The velocity deficit in the above-rated scenario did not cause the rotor speed to go below the rated rotor speed. The responses at higher frequencies were nearly identical, and the increase in fatigue loading (see Figure 19) can be attributed to the increase in low-frequency responses.

Figure 21 shows the differences in DELs for the tension in mooring line 2. The DELs in FWT2 tended to decrease for the below and rated scenarios and increase for the above-rated scenario (with some differences for the TLP where responses at higher frequencies were more influential). Mooring line responses were strongly correlated with surge motions; therefore, similar to tower bending, differences in structural loading between the three scenarios could largely be attributed to the velocity deficit and not meandering. These trends were not sensitive to inflow method nor turbulence level.

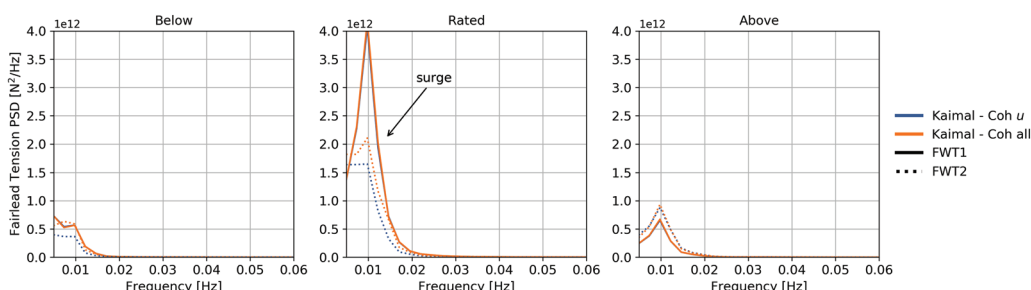


FIGURE 22 Mooring line 2 tension spectra of FWT1 and FWT2 for the semi in each wind speed scenario [Colour figure can be viewed at wileyonlinelibrary.com]

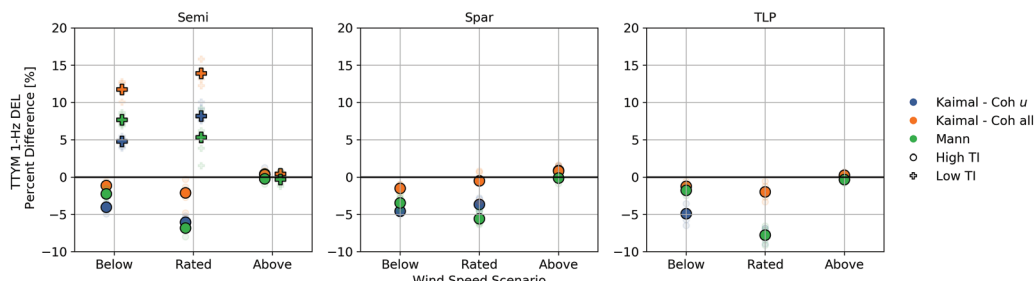


FIGURE 23 Tower top yaw moment percent difference in damage-equivalent load (DEL) between FWT1 and FWT2 for each wind speed scenario [Colour figure can be viewed at wileyonlinelibrary.com]

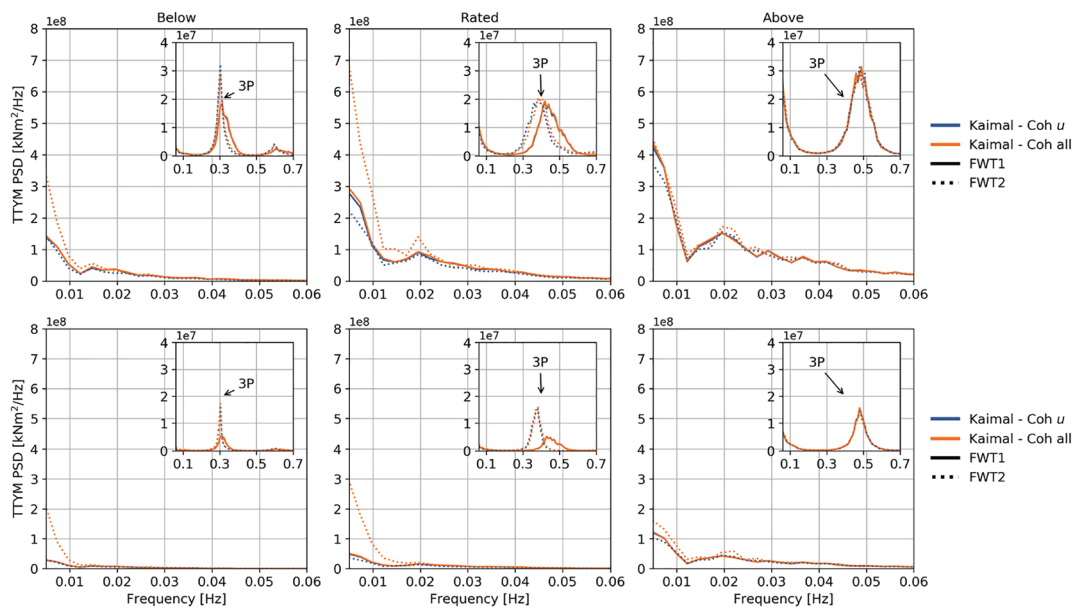


FIGURE 24 Tower top yaw moment spectra of FWT1 and FWT2 for the semi in each wind speed scenario for the higher turbulence (top) and lower turbulence (bottom) cases. Higher frequency responses are shown as an inset with a smaller vertical scale [Colour figure can be viewed at wileyonlinelibrary.com]

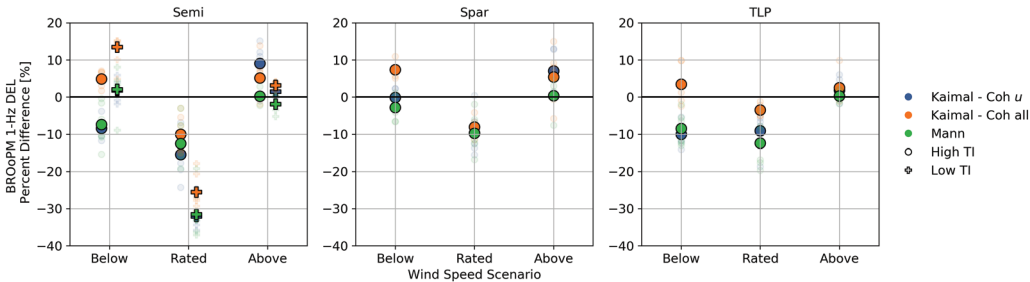


FIGURE 25 Blade root out-of-plane moment percent difference in damage-equivalent load (DEL) between FWT1 and FWT2 for each wind speed scenario [Colour figure can be viewed at wileyonlinelibrary.com]

Figure 22 shows the mooring line 2 tension spectra for the semi at low frequencies. Responses in the tension signal were at the surge natural frequency with the greatest response for the rated wind speed scenario. For the below and rated wind speed scenarios, the velocity deficit resulted in reduced response at the surge natural frequency for FWT2 compared with FWT1 resulting in less fatigue loading. The opposite was true for the above-rated scenario.

Figure 23 shows the percent differences in DELs for the tower top yaw moment moment of all three FWT concepts in each wind speed scenario. Fatigue loading in the high turbulence case decreased in the downstream turbine for the below and rated scenarios while it increased in the high turbulence case. Fatigue loading stayed roughly equivalent for the above scenario regardless of turbulence level.

When comparing the spectral response of the tower top yaw moment for Kaimal-Coh u and Kaimal-Coh all in Figure 24, it is clear that meandering significantly increased the low-frequency response. However, differences in DELs for the high turbulence case were dominated by the structural response due to 3P excitation. For the below and rated scenarios, the DEL decreased because the velocity deficit shifts the 3P excitation to a lower frequency. For the lower turbulence case, where responses at lower frequencies were more influential, meandering in Kaimal-Coh all resulted in 7.0% (below) and 5.8% (rated) greater DELs compared with Kaimal-Coh u .

The differences in DELs for the blade root out-of-plane bending moment in Figure 25 were due to both the velocity deficit and meandering. Figure 26 reveals that at lower frequencies, the blade root out-of-plane moment was correlated with the pitch motion while responses at higher frequencies were dominated at the 1P frequency. The velocity deficit affected the low-frequency dynamics as well as the frequency of the 1P excitation. Meandering increased response at the 1P frequency because the downstream turbine is subjected to partially waked conditions; ie, the blade encountered FWT1's wake once per rotation. This is evident by comparing the below and rated wind speed scenarios for Kaimal-Coh u and Kaimal-Coh all in Figure 26, where the responses at the 1P frequency for FWT2 were greater for Kaimal-Coh all than Kaimal-Coh u .

Figure 25 illustrates that the smaller velocity deficit and increased response at the 1P frequency due to meandering in Kaimal-Coh all led to increased fatigue loading for the below scenario. This trend was observed regardless of FWT concept and turbulence level. For the

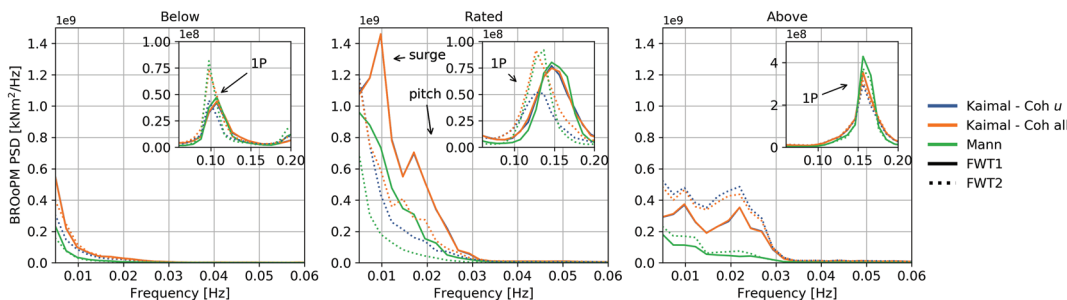


FIGURE 26 Blade root out-of-plane moment spectra of FWT1 and FWT2 for the semi in each wind speed scenario. Higher frequency responses are shown as an inset with a smaller vertical scale [Colour figure can be viewed at wileyonlinelibrary.com]

high TI case, fatigue loading increased between 3% and 7% depending on FWT concept. For the low TI case, fatigue loading for the semi increased 13.5% for Kaimal-Coh all. For the rated scenario, there was less of a decrease in fatigue loading for Kaimal-Coh all compared with Kaimal-Coh *u*. Since there is minimal meandering in the above wind speed scenario, differences in low-frequency response were more influential to differences in fatigue loading resulting in increased fatigue loading, between 1% and 10% for the Kaimal turbulence model depending on FWT concept, as a result of the velocity deficit. However, the trends for Mann were slightly different: The DEL decreased for both the below and rated scenarios while it stayed the same for the above scenario, due to the effects of loads at higher frequencies (see Figure 26).

5 | CONCLUSIONS

To investigate how wake meandering affects the platform motions and structural loading of FWTs, simulations were performed for three different 10-MW FWT concepts (a semisubmersible, a spar, and a TLP) in a mid-fidelity wind farm modeling tool. This tool, FAST.Farm, uses instances of OpenFAST, an aero-hydro-servo-elastic tool that is commonly used in the structural design process of multimegawatt wind turbines. A simple two-turbine case where the downstream turbine was separated by 8D in the wind direction was considered.

Three different wind speed scenarios and two different turbulence levels were included. The wind fields were synthesized in three ways: The first method, Kaimal-Coh *u*, used the Kaimal model with spatial coherence specified in the longitudinal velocity component only (as prescribed in the IEC 61400-1 standard¹²); the second method, Kaimal-Coh all, also used the Kaimal model but had spatial coherence specified in the longitudinal, lateral, and vertical velocity components; and the third method, Mann, used the Mann model which had spatial coherence in all three velocity components inherent in the model. Kaimal-Coh *u* resulted in a uniform wake deficit with negligible meandering. For Kaimal-Coh all and Mann, lateral meandering decreased with increasing wind speed but occurred at higher frequencies. Additionally, there was less meandering for the lower of the two turbulence levels. Similar to previous work,²⁹ Kaimal-Coh all resulted in greater lateral meandering that occurred at higher frequencies compared to Mann. An investigation of the Kaimal-Coh all and Mann inflow methods revealed that the lateral velocity component in Kaimal-Coh all had greater energy content and coherence for intermediate and large lateral separation distances (relative to the size of the rotor) at low frequencies compared with Mann. Lateral meandering was not sensitive to the specific FWT concept; however, vertical meandering did differ by platform. The spar's wake deflected to a higher vertical location as it operated at a greater mean pitch angle compared with the semisubmersible and TLP. This resulted in the spar having the smallest velocity deficit.

Lateral wake meandering significantly increased platform yaw motions in the downstream FWTs compared with the upstream FWTs. For the semi, which has a very low yaw natural frequency that was excited by meandering, yaw motion standard deviations increased by close to 40% at rated and lower wind speeds. The spar and TLP still saw quasi-static increases in yaw motion standard deviations of close to 20%. For the lower turbulence level, yaw motion standard deviations for the downstream semi more than doubled. Surge and pitch motions were not susceptible to wake meandering and depended mainly on the velocity deficit.

Fatigue due to four global load effects, the tension of mooring lines, the tower base fore-aft bending moment, the tower top yaw moment, and the blade root out-of-plane moment, was examined. Differences in DELs in the mooring lines and tower base for the upstream turbine compared with the downstream turbine were mainly driven by the incoming wind speed. Fatigue tended to increase for the below- and above-rated wind speeds and decrease for the rated wind speed, though the results depended on the tower natural frequency. At the tower top, trends did not depend on FWT concept: Meandering affected the low-frequency structural loading, but the DELs were dominated by responses due to 3P excitation. This resulted in decreased fatigue loading in rated and below wind speeds. However, for the lower turbulence level where low-frequency loading was more influential, meandering increased the DEL by 5% to 7%. In the blade root, the DEL was sensitive to both the velocity deficit at low frequencies and meandering at the 1P frequency. For the Kaimal turbulence model, meandering led to increased fatigue for the below-rated wind speed and the velocity deficit led to increased fatigue for the above-rated wind speed regardless of FWT concept. For the Mann model, the trends were not as clear because low-frequency structural loading was less influential compared with load effects at higher frequencies.

Many previous studies have found that the wake effects lead to increased fatigue loading.³⁻⁷ These classical studies have examined rotor and/or blade loading for onshore or bottom-fixed offshore wind turbines. In the present work, we find that for FWTS, the effects of slowly varying loads, especially inertia loads, are so important (even for blade loading) that wake effects do not necessarily lead to increased fatigue loading at rated wind speed. Low-frequency resonant responses at a given ambient or waked wind speed are more important drivers for determining fatigue.

The present work aims to provide insight into the role of wake interaction within floating wind farms. The approach extends standard methods used for the design of single wind turbines to wind farm simulation. This study, along with several preceding studies, demonstrates the sensitivity of floating wind turbine wind farm dynamics to the industry-accepted inflow methods. Further research, including high-resolution offshore wind field measurements, or high-fidelity simulations, is needed in order to better understand how these models compare with reality.

ACKNOWLEDGEMENTS

The first author acknowledges support from the US-Norway Fulbright Foundation. Discussions with Lene Eliassen and Marit Kvitem of SINTEF Ocean and Jason Jonkman and Kelsey Shaler of NREL are also appreciated.

ORCID

Adam S. Wise  <https://orcid.org/0000-0002-7234-6014>

Erin E. Bachynski  <https://orcid.org/0000-0002-1471-8254>

REFERENCES

1. Statoil. Hywind Scotland Pilot Park. <http://www.statoil.com/en/TechnologyInnovation/NewEnergy/RenewablePowerProduction/Offshore/HywindScotland>; 2014.
2. S. Lissaman PB. Energy effectiveness of arbitrary arrays of wind turbines. *J Energy*. 1979;3(6):323-328. <https://doi.org/10.2514/3.62441>
3. Taylor GJ. Wake measurements on the Nibe wind turbines in Denmark. CEC Contract EN3W.0039.UK(H1); 1990.
4. Thomsen K, Sørensen P. Fatigue loads for wind turbines operating in wakes. *J Wind Eng Ind Aerod*. 1999;80(1-2):121-136. [https://doi.org/10.1016/S0167-6105\(98\)00194-9](https://doi.org/10.1016/S0167-6105(98)00194-9)
5. Frandsen S, Christensen C. Structural loads in large wind farm arrays. In: European Wind Energy Conference and Exhibition, EWEC '94; 1994. Conference date: 09-10-1994 Through 13-10-1994; 1994.
6. Frandsen S, Thomsen K. Change in fatigue and extreme loading when moving wind farms offshore. *Wind Engineering*. 1997;21(3):197-214.
7. Dahlberg J, Poppen M, Thor S. Load/fatigue effects on a wind turbine generator in a wind farm. *J Wind Eng Ind Aerod*. 1992;39(1):199-209. [https://doi.org/10.1016/0167-6105\(92\)90546-M](https://doi.org/10.1016/0167-6105(92)90546-M)
8. Ainslie J. Calculating the flowfield in the wake of wind turbines. *J Wind Eng Ind Aerod*. 1988;27(1-3):213-224. [https://doi.org/10.1016/0167-6105\(88\)90037-2](https://doi.org/10.1016/0167-6105(88)90037-2)
9. Churchfield M, Wang Q, Scholbrock A, Herges T, Mikkelsen T, Sjöholm M. Using high-fidelity computational fluid dynamics to help design a wind turbine wake measurement experiment. *J Phys: Conf Ser*. 2016;753:032009. <https://doi.org/10.1088/1742-6596/753/3/032009>
10. Keck RE, Maré dM, Churchfield MJ, Lee S, Larsen G, Madsen HA. On atmospheric stability in the dynamic wake meandering model. *Wind Energy*. 2014;17(11):1689-1710. <https://doi.org/10.1002/we.1662>
11. Larsen GC, Madsen HA, Thomsen K, Larsen TJ. Wake meandering: a pragmatic approach. *Wind Energy*. 2008;11(4):377-395. <https://doi.org/10.1002/we.267>
12. International Electrotechnical Commission (IEC). Wind turbines: part 1: design requirements. Tech. Rep IEC 61400-1; 2019.
13. Larsen T, Hansen A. Risø National Lab, DTU WED. How 2 HAWC2, The User's Manual. Tech. Rep OCLC: 826677469; 2007.
14. Madsen HA, Larsen GC, Larsen TJ, Troldborg N, Mikkelsen R. Calibration and validation of the dynamic wake meandering model for implementation in an aeroelastic code. *J Sol Energ*. 2010;132(4):041014. <https://doi.org/10.1115/1.4002555>
15. Jonkman JM, Annoni J, Hayman G, Jonkman B, Purkayastha A. Development of FAST. Farm: A New Multi-Physics Engineering Tool for Wind—2 Design and Analysis. In: Grapevine, Texas: American Institute of Aeronautics and Astronautics; 2017.
16. Jonkman J, Buhl M. FAST User'S Guide. Golden, CO: National Renewable Energy Laboratory; 2005. NREL/EL-500-38230.
17. Jonkman J, Doubrava P, Hamilton N, Annoni J, Fleming P. Validation of FAST, farm against large-eddy simulations. *J Phys: Conf Ser*. 2018;1037:062005. <https://doi.org/10.1088/1742-6596/1037/6/062005>
18. Doubrava P, Annoni JR, Jonkman JM. Optimization-based calibration of FAST.Farm parameters against large-eddy simulations. In: American Institute of Aeronautics and Astronautics; 2018; Kissimmee, Florida.
19. Jiménez A, Crespo A, Migoya E. Application of a LES technique to characterize the wake deflection of a wind turbine in yaw. *Wind Energy*. 2009;13(6):559-572. <https://doi.org/10.1002/we.380>
20. Jonkman JM. FAST.Farm User's Guide and Theory Manual. Golden, CO: National Renewable Energy Laboratory. NREL/TP-xxxxx.
21. Kaimal JC, Wyngaard JC, Izumi Y, Coté OR. Spectral characteristics of surface-layer turbulence. *Q J R Meteorol Soc*. 1972;98(417):563-589. <https://doi.org/10.1002/qj.49709841707>
22. Mann J. The spatial structure of neutral atmospheric surface-layer turbulence. *J Fluid Mech*. 1994;273:141-168.
23. Mann J. Wind field simulation. *Probabilistic Eng Mech*. 1998;13(4):269-282.
24. Bachynski EE, Eliassen L. The effects of coherent structures on the global response of floating offshore wind turbines. *Wind Energy*. 2018;0(0):1-20. <https://doi.org/10.1002/we.2280>

25. Eliassen L, Bachynski EE. *The Effect of Turbulence Modelling on the Response of a Large Floating Wind Turbine*, No. OMAE2017-61179 in ASME 2017 36th International Conference on Ocean, Offshore and Arctic Engineering. Trondheim, Norway; 2017.
26. Godvik M. *Influence of the Wind Coherence on the Response of a Floating Wind Turbine*, Science meets Industry. Stavanger; 2016.
27. Doubrawa P, Churchfield MJ, Godvik M, Sirnivas S. Load response of a floating wind turbine to turbulent atmospheric flow. *Applied Energy*. 2019;242:1588-1599. <https://doi.org/10.1016/j.apenergy.2019.01.165>
28. Shaler K, Jonkman J, Doubrawa P, Hamilton N. FAST.Farm response to varying wind inflow techniques. In: American Institute of Aeronautics and Astronautics; 2019; San Diego, California.
29. Wise A, Bachynski EE. Analysis of wake effects on global responses for a floating two-turbine case. *J Phys: Conf Ser*. 2019;1356:012004. <https://doi.org/10.1088/1742-6596/1356/1/012004>
30. International Electrotechnical Commission (IEC). Wind turbines: part 3: design requirements for offshore wind turbines. Tech. Rep IEC 61400-3; 2009.
31. Hall M. *MoorDyn User's Guide*. Orono, ME: Department of Mechanical Engineering, University of Maine; 2015.
32. Shaler K, Jonkman J, Hamilton N. Effects of inflow spatiotemporal discretization on wake meandering and turbine structural response using FAST.Farm. *J Phys: Conf Ser*. 2019;1256(012023). <https://doi.org/10.1088/1742-6596/1256/1/012023>
33. Bak C, Zahle F, Bitsche R, et al. Description of the DTU 10 MW reference wind turbine. Tech. Rep. DTU Wind Energy Report-I-0092, DTU Wind Energy; 2013.
34. Pegalajar-Jurado A, Madsen FJ, Borg M, Bredmose H. Public definition of the two LIFES 50+ 10MW floater concepts. Tech. Rep. D4.2, Lifes50+; 2018.
35. Pegalajar-Jurado A, Madsen FJ, Borg M, Bredmose H. State-of-the-art models for the two LIFES 50+ 10MW floater concepts. Tech. Rep. D4.5, Lifes50+; 2018.
36. Design XueW, modelling numerical. Analysis of a spar floater supporting the DTU 10m MW wind turbine. Master's thesis NTNU; 2016.
37. Design TX, Modelling Numerical. Analysis of TLP floater supporting the DTU 10 MW wind turbine. Master's thesis NTNU; 2016.
38. Thiagarajan KP, Dagher HJ. A review of floating platform concepts for offshore wind energy generation. *J Offshore Mech Arct Eng*. 2014;136(2):020903. <https://doi.org/10.1115/1.4026607>
39. Larsen T, Hanson T. A method to avoid negative damped low frequent tower vibrations for a floating, pitch controlled wind turbine. *J Phys: Conf Ser, The Second Conference on The Science of Making Torque from Wind*. 2007;75.
40. Galvan J, Sánchez-Lara M, Mendikoa I, et al. Definition and analysis of NAUTILUS-DTU10 MW floating offshore wind turbine at Gulf of Maine. Experiments at Sintef Ocean & PoliMi. Tech. Rep. TRI-ORE-PUB-001/2017, Tecnalia Research & Innovation; 2017.
41. Jonkman J. Definition of the floating system for phase IV of OC3. Tech. Rep. NREL/TLP-500-47535; 2010.
42. Hsu CG. Substructure models for dynamic analysis of floating wind turbines and the effect of hull flexibility. Master's thesis NTNU/TU Delft; 2019.
43. Bachynski E, Moan T. Design considerations for tension leg platform wind turbines, marine structures. 2012;29:89-114. <https://doi.org/10.1016/j.marlstruc.2012.09.001>
44. Li L, Gao Z, Moan T. Joint environmental data at five European offshore sites for design of combined wind and wave energy concepts. In: No. OMAE 2013-10156 in 32nd International Conference on Ocean, Offshore, and Arctic Engineering; 2013.
45. Türk M, Emeis S. The dependence of offshore turbulence intensity on wind speed. *J Wind Eng Ind Aerod*. 2010;98(8-9):466-471. <https://doi.org/10.1016/j.jweia.2010.02.005>
46. Jonkman B. *TurbSim User's Guide v2.00.00*. Tech. Rep. Golden CO; 2014. NREL/TP-xxxxx, National Renewable Energy Laboratory.
47. DTU Wind Energy, Pre-processing tools—HAWC2. <http://www.hawc2.dk/download/pre-processing-tools>; 2014.
48. Smedman AS. Some additional coherence data in the inertial subrange. *J Clim Appl Meteorol*. 1987;26(12):1770-1773. [https://doi.org/10.1175/1520-0450\(1987\)026<1770:SACDIT>2.0.CO;2](https://doi.org/10.1175/1520-0450(1987)026<1770:SACDIT>2.0.CO;2)
49. Kristensen L, Jensen NO. Lateral coherence in isotropic turbulence and in the natural wind. *Boundary-Layer Meteorol*. 1979;17(3):353-373. <https://doi.org/10.1007/BF00117924>
50. Hayman G, Buhl M. *MLife User's Guide for Version 1.00. Technical Report NREL/TP-XXXXX*. Golden CO; 2012. National Renewable Energy Laboratory.
51. Gebraad PMO, Teeuwisse FW, Wingerden vJW, et al. Wind plant power optimization through yaw control using a parametric model for wake effects—a CFD simulation study: wind plant optimization by yaw control using a parametric wake model. *Wind Energy*. 2016;19(1):95-114. <https://doi.org/10.1002/we.1822>
52. Chougule A, Mann J, Kelly M, Sun J, Lenschow DH, Patton EG. Vertical cross-spectral phases in neutral atmospheric flow. *J Turbul*. 2012;13(N36). <https://doi.org/10.1080/14685248.2012.711524>
53. Passon P, Kühn M, Butterfield S, Jonkman J, Camp T, Larsen TJ. OC3-Benchmark exercise of aero-elastic offshore wind turbine codes. *J Phys: Conf Ser*. 2007;75:012071. <https://doi.org/10.1088/1742-6596/75/1/012071>
54. Zahle F, Bitsche R, et al. The DTU 10-MW reference wind turbine, 22; 2013.

How to cite this article: Wise A, Bachynski EE. Wake meandering effects on floating wind turbines. *Wind Energy*. 2020;1–20. <https://doi.org/10.1002/we.2485>

APPENDIX A: READING OF MANN WIND FIELDS IN THE AEROELASTIC CODES

The Mann model includes uniform wind shear. The uniform, linear wind shear results in eddies first arriving at a higher vertical location and then at lower vertical location (z_a and z_b in Figure A1, respectively). Eddies first arriving at higher vertical locations has been observed in nature and

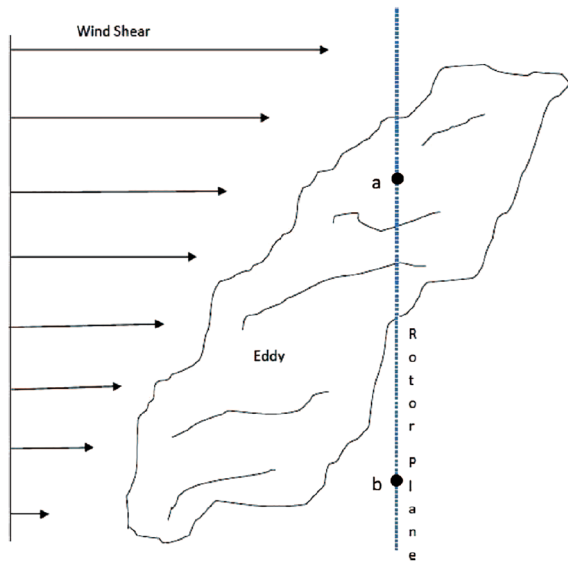


FIGURE A1 Eddy schematic. Image from Chougule et al⁵² [Colour figure can be viewed at wileyonlinelibrary.com]

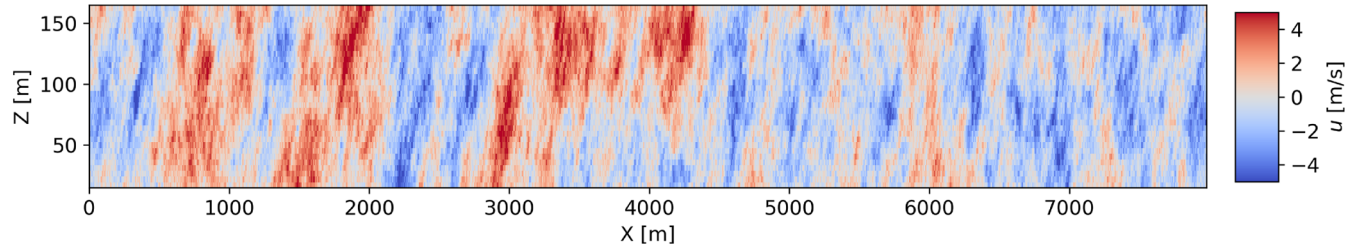


FIGURE A2 Raw Mann wind field [Colour figure can be viewed at wileyonlinelibrary.com]

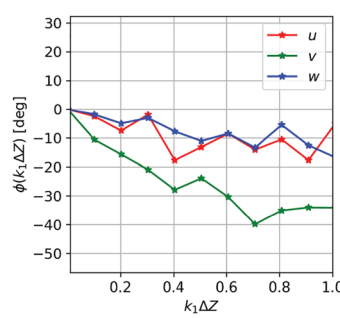
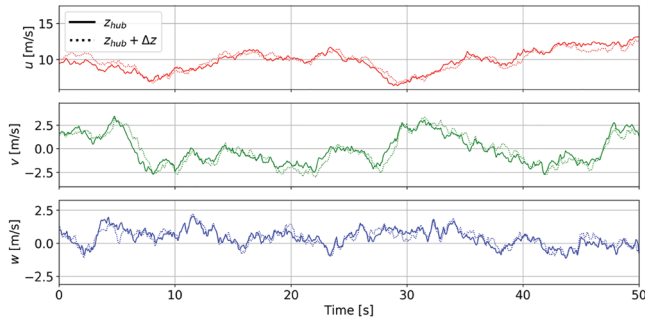


FIGURE A3 Time series (left) and spectral phases (right) for all three velocity components of the OC3 wind. Outputs are from OpenFAST v0.1.0 [Colour figure can be viewed at wileyonlinelibrary.com]

LES.⁵² As seen in Figure A2, the preprocessed 11.4-m/s Mann wind field generated using the IEC turbulence simulator for the Offshore Code Comparsion Collaboration (OC3)⁵³ also demonstrates turbulent eddies being stretched from lower z and x to higher z and x . Assuming Taylor's hypothesis of frozen turbulence is valid, then the spatial and temporal domains can be related such that $t = x/\bar{u}$ and $k_1 = 2\pi f/\bar{u}$. Therefore, Figures A1 and A2 are in agreement assuming the wind propagation direction in both figures is from the left to the right. In other words, a wind turbine at the right of Figure A2 should first see the YZ slice at $x = 7980$ m and then from $x \approx 7979$ m and so on.

However, the preprocessed wind field shown in Figure A2 is not equivalent to the wind field seen by wind turbines in many aeroelastic codes. On the basis of many code-to-code comparisons (OC3, for example), HAWC2, FAST, FAST.Farm, SIMA, and other aeroelastic codes all read the Mann wind in the same way. The aeroelastic codes read the wind fields with increasing x ; ie, the wind turbine is on the left of Figure A2, and wind propagates from the right to the left, resulting in turbulent eddies arriving first at lower z . This phenomenon can be described mathematically by calculating the phases ϕ between two vertically separated time series i and j . The phase can be calculated from the complex cross-spectra C_{ij} :

$$C_{ij}(f, \Delta Z) = \hat{u}_i(f, z_a)\hat{u}_j^*(f, z_b), \quad (A1)$$

$$\phi_{ij}(f, \Delta Z) = \arg(C_{ij}(f, \Delta Z)), \quad (A2)$$

where f is frequency, $\Delta Z = z_a - z_b$, $\hat{u}_i(f, z_a)$ is the complex-valued Fourier transform of the i th velocity component $u_i(t)$ at height z_a and $*$ denotes complex conjugate.

The OC3 wind field was fed through OpenFAST v0.1.0, and time series of the wind field velocity components at $z_{hub} = 90$ m and $z_{hub} + \Delta z = 94.6875$ m were obtained. The phases calculated in Figure A3 show that time series at $z_{hub} + \Delta z$ lag compared with z_{hub} for all three velocity components. This can also be observed qualitatively by looking at the time series in Figure A3.

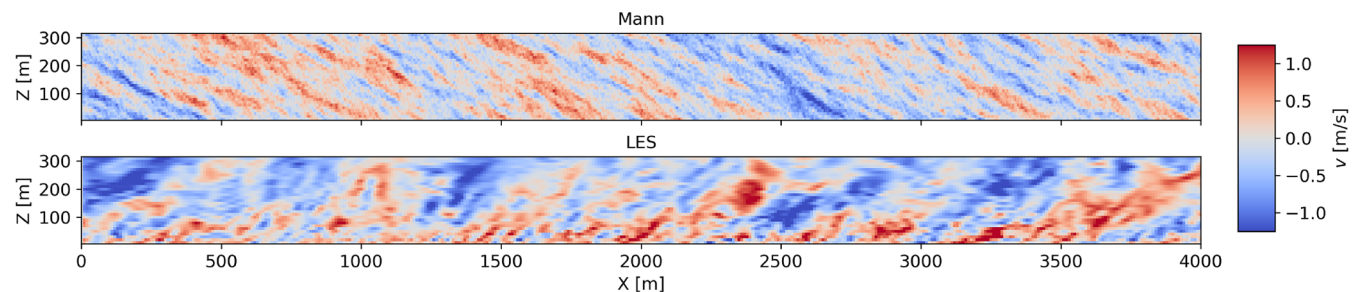


FIGURE A4 Lateral velocity component FAST.Farm outputs for Mann wind and wind generated from a large-eddy simulation (LES) precursor (neutral atmospheric stability, 8 m/s, 10% TI case in Jonkman et al¹⁷) [Colour figure can be viewed at wileyonlinelibrary.com]

Figure A3 reveals that the phase lag is most obvious in the v -velocity component. Lateral velocity component (unmodified official version) FAST.Farm vtk outputs for Mann wind and wind generated from an LES precursor for the same wind speed, turbulence, and shear exponent are compared in Figure A4. It is clear that the eddies are stretched in opposite direction for Mann compared with LES (wind propagation is in the positive x -direction). In the present work, FAST.Farm and OpenFAST are modified to read the files in the opposite direction compared to the official versions to correct this apparent error.